



**HAL**  
open science

## High-temperature deformation of enstatite aggregates

M. Bystricky, J. Lawlis, S. Mackwell, F. Heidelbach, P. Raterron

► **To cite this version:**

M. Bystricky, J. Lawlis, S. Mackwell, F. Heidelbach, P. Raterron. High-temperature deformation of enstatite aggregates. *Journal of Geophysical Research: Solid Earth*, 2016, 121, pp.6384-6400. 10.1002/2016JB013011 . insu-03669433

**HAL Id: insu-03669433**

**<https://insu.hal.science/insu-03669433>**

Submitted on 17 May 2022

**HAL** is a multi-disciplinary open access archive for the deposit and dissemination of scientific research documents, whether they are published or not. The documents may come from teaching and research institutions in France or abroad, or from public or private research centers.

L'archive ouverte pluridisciplinaire **HAL**, est destinée au dépôt et à la diffusion de documents scientifiques de niveau recherche, publiés ou non, émanant des établissements d'enseignement et de recherche français ou étrangers, des laboratoires publics ou privés.

Copyright

## RESEARCH ARTICLE

10.1002/2016JB013011

## Key Points:

- We performed high-temperature deformation experiments on polycrystalline enstatite in the protoenstatite and the orthoenstatite fields
- A dislocation creep flow was determined for orthoenstatite with a stress exponent of 3 and an activation energy of 600 kJ/mol
- Orthoenstatite is stronger than olivine by a factor of 2 in experiments, but the strength contrast is likely lower at natural conditions

## Correspondence to:

M. Bystricky,  
mbystricky@irap.omp.eu

## Citation:

Bystricky, M., J. Lawlis, S. Mackwell, F. Heidelbach, and P. Raterron (2016), High-temperature deformation of enstatite aggregates, *J. Geophys. Res. Solid Earth*, 121, 6384–6400, doi:10.1002/2016JB013011.

Received 21 MAR 2016

Accepted 21 AUG 2016

Accepted article online 23 AUG 2016

Published online 17 SEP 2016

## High-temperature deformation of enstatite aggregates

M. Bystricky<sup>1</sup>, J. Lawlis<sup>2</sup>, S. Mackwell<sup>2,3</sup>, F. Heidelbach<sup>4</sup>, and P. Raterron<sup>5</sup>

<sup>1</sup>IRAP, UPS, CNRS, Université de Toulouse, Toulouse, France, <sup>2</sup>Department of Geosciences, Pennsylvania State University, University Park, Pennsylvania, USA, <sup>3</sup>Lunar and Planetary Institute, Houston, Texas, USA, <sup>4</sup>Bayerisches Geoinstitut, Universität Bayreuth, Bayreuth, Germany, <sup>5</sup>UMET, CNRS/Université de Lille, Villeneuve d'Ascq CEDEX, France

**Abstract** Synthesized polycrystalline enstatite samples were deformed in a Paterson gas-medium apparatus at 1200–1300°C, oxygen fugacity buffered at Ni/NiO, and confining pressures of 300 MPa (protoenstatite field) or 450 MPa (orthoenstatite field). At both confining pressures, the mechanical data display a progressive increase of the stress exponent from  $n = 1$  to  $n \sim 3$  with increasing differential stress, suggesting a transition from diffusional to dislocation creep. Nonlinear least squares fits to the high-stress data yielded dislocation creep flow laws with a stress exponent of 3 and activation energies of 600 and 720 kJ/mol for orthoenstatite and protoenstatite, respectively. Deformed samples were analyzed using optical microscopy and scanning and transmission electron microscopy. Microstructures show undulatory extinction and kink bands, evidence of dislocation processes. Crystallographic preferred orientations measured by electron backscatter diffraction are axisymmetric and indicate preferential slip on (100)[001]. Most deformed grains comprise an interlayering of orthoenstatite and clinoenstatite lamellae. While many lamellae may have formed during quenching from run conditions, those in samples deformed in the orthoenstatite field are often bordered by partial [001] dislocations, suggesting transformation due to glide of partial [001] dislocations in (100) planes. Comparison of our orthoenstatite creep law with those for dislocation creep of olivine indicates that orthoenstatite deforms about a factor of 2 slower than olivine at our experimental conditions. However, as orthoenstatite has a higher activation energy and smaller stress exponent than olivine, this strength difference is likely smaller at the higher temperatures and lower stresses expected in much of the upper mantle.

### 1. Introduction

The minerals olivine, orthopyroxene, clinopyroxene, and garnet comprise the bulk of the upper mantles of Earth and the other terrestrial planets. As olivine is the most abundant and arguably the weakest of these minerals under upper mantle conditions, significant effort has been expended in understanding its mechanical behavior [see, e.g., Carter and Avé Lallemant, 1970; Chopra and Paterson, 1981, 1984; Zeuch and Green, 1984; Mackwell et al., 1985; Karato et al., 1986; Borch and Green, 1989; Hirth and Kohlstedt, 1995a, 1995b; Bystricky et al., 2000; Mei and Kohlstedt, 2000a, 2000b; Karato and Jung, 2003; Durham et al., 2009; Raterron et al., 2009; Keefner et al., 2011]. Due to the importance of clinopyroxene in crustal lithologies, a number of studies have also investigated the mechanical behavior of clinopyroxene single crystals and polycrystals [e.g., Avé Lallemant, 1978; Kollé and Blacic, 1982, 1983; Kirby and Kronenberg, 1984; Boland and Tullis, 1986; Raterron and Jaoul, 1991; Ingrin et al., 1991, 1992; Raterron et al., 1994; Jaoul and Raterron, 1994; Mauler et al., 2000; Bystricky and Mackwell, 2001; Hier-Majumder et al., 2005; Chen et al., 2006; Amiguet et al., 2009, 2010]. However, much less attention has been given to the other important mantle minerals, orthopyroxene and garnet, partly due to their perceived lesser contribution to creep in the convecting mantle; to the unavailability of suitable clean, single-phase materials for study (orthopyroxene); and/or to their stability under conditions available for quantitative deformation experiments (garnet and, to a lesser extent, orthopyroxene).

As the second most abundant mineral in Earth's convecting upper mantle and a dominant mineral in zones within the depleted lithosphere and in ophiolites, orthopyroxene with a composition near  $(\text{Mg}_{0.9}\text{Fe}_{0.1})_2\text{Si}_2\text{O}_6$  (i.e., enstatite) will exert an important influence on the mechanical behavior of the convecting mantle and lithosphere. Previous work on natural orthopyroxene aggregates in high-pressure Griggs' deformation apparatus under reported "dry" [Raleigh et al., 1971] and "wet" [Ross and Nielsen, 1978] conditions provided useful information on dislocation creep processes, showing that deformation at temperatures greater than 1000°C and confining pressures of 1–2 GPa primarily involves the (100)[001] slip system. These studies also observed

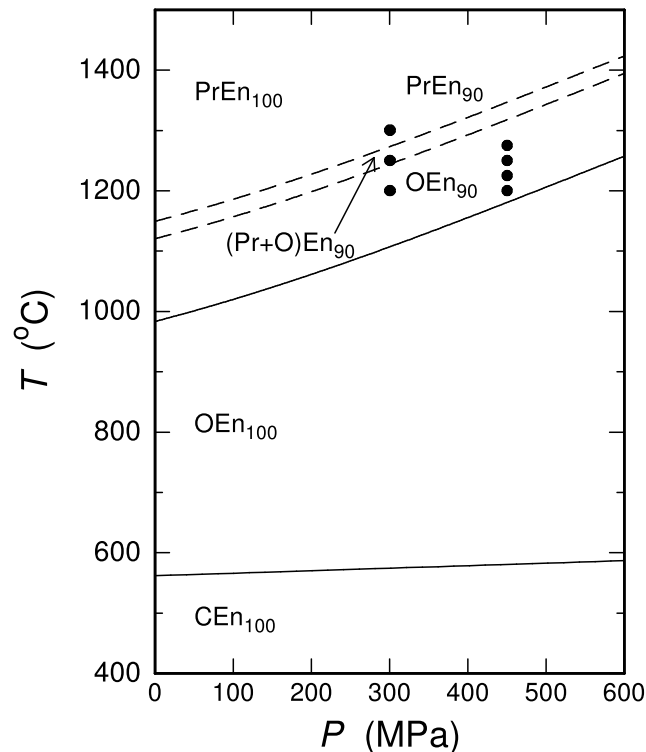


**Figure 1.** Plot of the stability fields for enstatite, showing the stability ranges for orthoenstatite (O), low clinoenstatite (C), and protoenstatite (Pr). The  $En_{100}$  fields are bounded by the solid lines, which are taken from the synthesis of Gasparik [2003, p. 26]. The  $En_{90}$  ( $En_{90}Fs_{10}$ ) fields are bounded by the dashed lines, which are derived from the  $En_{100}$  curves using the room pressure phase relations compiled in Huebner [1980, p. 239]. The points are the conditions of our experiments, not allowing for an effect of applied stress on total pressure.

aggregates. They report a reduction in the strength of both orthopyroxene and olivine aggregates under more oxidizing deformation conditions. Lawlis [1998] performed experiments on enstatite and olivine-enstatite aggregates at 300 and 450 MPa confining pressure; his results for enstatite aggregates are reported here. Ji *et al.* [2001] deformed pure Mg-enstatite ( $MgSiO_3$ ) aggregates at room pressure and 1423–1593 K over a range of oxygen fugacities in the protoenstatite stability field (see the stability field diagram in Figure 1). Their samples were considerably weaker than those of Hitchings *et al.* [1989] and yielded  $n = 2.0$  and  $Q = 584$  kJ/mol, suggesting a component of diffusional creep or grain boundary sliding. Studies by McDonnell *et al.* [2000] and Sundberg and Cooper [2008] on two-phase enstatite-olivine aggregates focused more on deformation in the grain boundary sliding or diffusional creep fields.

Experiments have also been performed on single crystals of enstatite to characterize behavior of individual slip systems. Schloessin and Ranalli [1988] performed room pressure three-point bending experiments on single crystals from Bamble, Norway, at high temperatures to demonstrate the capability of the technique at low stresses. Mackwell [1991] performed uniaxial experiments on orthopyroxene single crystals oriented to favor slip on the easiest dislocation slip systems at high temperatures in a room pressure deformation apparatus (i.e., in the protoenstatite stability field). His results demonstrate that enstatite deformation does not have the dependence on oxygen fugacity that is observed for olivine single crystals and give strengths that are significantly higher than for the easier slip systems in olivine under comparable conditions. Ohuchi *et al.* [2011] performed experiments on oriented single crystals of enstatite at a confining pressure of 1.3 GPa and temperatures from 973 to 1373 K in a Griggs' high-pressure deformation apparatus. Their measurements, which they reported to be in the low clinoenstatite field, yield a stress exponent of  $n = 3$  and activation energy of  $Q = 459$  kJ/mol for high-temperature deformation on the (100)[001] slip system. These results are much weaker than those of Mackwell [1991] for protoenstatite and are also somewhat weaker than those for dry deformation

subgrain formation and syntectonic recrystallization. It is likely that none of these experiments were performed under truly dry conditions, as evidenced by similar creep strengths in the two studies and measurements of a stress exponent of  $n = 2.4$  and an activation energy for creep of  $Q = 290$  kJ/mol by Raleigh *et al.* [1971] and  $n = 2.8$  and  $Q = 270$  kJ/mol by Ross and Nielsen [1978].

Dehghan *et al.* [1981, 1982] reported preliminary results for hot-pressed aggregates formed from ground single crystals of orthopyroxene from Bamble, Norway. Their room pressure study showed similar strengths to those of Raleigh *et al.* [1971], with  $n = 3.6$  for "reducing" and  $n = 2.9$  for "nonreducing" conditions. Hitchings *et al.* [1989] prepared both monomineralic and two-phase samples from powders of orthopyroxene and olivine separated from spinel lherzolite nodules. At 300 MPa confining pressure, 1500 K, and with the oxygen fugacity buffered at Fe/FeO, their orthopyroxenite samples yielded a stress exponent of  $n \approx 3.0$  and were slightly stronger than pure olivine

of olivine single crystals and polycrystals. Recently, *Raterron et al.* [2016] reported results of deformation experiments on oriented enstatite single crystals at confining pressures of 3–6 GPa and temperatures from 1313 to 1645 K. They concluded that the orthopyroxene (100)[001] slip system is weaker than the (010)[001] slip system and that both orthopyroxene slip systems are significantly stronger than olivine slip systems.

## 2. Experimental Techniques and Procedures

### 2.1. Starting Material

Synthetic enstatite was produced by reacting fine-grained quartz and olivine powders at high temperature. Laboratory-grade (99.999% purity) quartz powders and olivine single crystals from San Carlos, AZ, with compositions near  $(\text{Mg}_{0.906}\text{Fe}_{0.091}\text{Ni}_{0.003})\text{SiO}_4$  were selected as the source material. The olivine crystals were optically transparent and 5–20 mm in diameter. They were hand-selected to exclude accessory minerals such as spinel or pyroxene and were broken into millimeter-size fragments in a steel crusher. Olivine and quartz powders were ground separately using an agate mortar and pestle and sieved to yield grain sizes below 45  $\mu\text{m}$ . Both were further ground for 1 h in a micronizing mill containing agate cylinders and distilled water. Micronized powders were then gravitationally settled in distilled water to obtain powder batches with a particle-size range of 0–10  $\mu\text{m}$ . The fine-grained powders were dried in an oven at 250°C for at least 24 h.

These fine-grained olivine and quartz powders were weighed and mixed in equal molar ratios and ground in distilled water using an agate mortar and pestle to evenly distribute the quartz and olivine grains. The mixtures were placed in a crucible made from Mt. Burnet dunite composed of a 2 mm thick disk and a hollow cylinder (30 mm outer diameter, 20 mm inner diameter, and 45 mm height), which had been prebaked at 1 atm, 1000°C, and an oxygen fugacity of  $10^{-10}$  atm to remove any hydrous species. In most cases (PI-339, PI-512, and PI-539), this configuration provided a slight excess in olivine during the synthesis and buffered the activity of  $\text{SiO}_2$  in the enstatite at olivine-normative conditions. It also eliminated any potential contamination due to use of an alumina or zirconia crucible. In the case of PI-402, excess quartz in the starting powders resulted in an enstatite sample that was quartz normative.

The mixed powders were reacted in the crucibles at 1430°C for 150 h in a 1 atm furnace under controlled oxygen fugacity conditions near Ni/NiO ( $10^{-5.5}$  atm) using CO/CO<sub>2</sub> gas mixtures. Subsequently, the reacted powders were ground one more time in distilled water in an agate mortar and pestle and were reacted under the same conditions for an additional 100 h to ensure that the reaction was complete. Microprobe analysis showed that the resulting enstatite powder was homogeneous in composition ( $\text{En}_{91}$ ), and X-ray powder diffraction confirmed that its structure was monoclinic (low clinoenstatite). The powders were subsequently stored in a vacuum oven at 150°C to minimize water contamination.

### 2.2. Sample Fabrication

In order to prepare fully dense polycrystalline samples the enstatite powders were cold pressed at a uniaxial stress of 200 MPa in a nickel sleeve (10 mm inner diameter and 20 mm height) with a hardened steel cold-pressing die. The nickel-jacketed cold-pressed samples were loaded into an internally heated gas-medium pressure vessel and hot pressed for 2–12 h at 1300°C and a confining pressure of 300 MPa (for experiments in the protoenstatite stability field) or 450 MPa (for experiments in the orthoenstatite stability field; Table 1 and Figure 1).

Porosities in the hot-pressed samples were less than 2%, as measured using the Archimedeian method. The samples were cored to a diameter of 8 mm and ground to a length of 14–16 mm for the deformation experiments. In order to remove any hydrous species that may have been trapped during the hot-pressing stage, the samples were subsequently annealed for 20 h at 1 atm and 1000°C under controlled oxygen fugacity conditions near Ni/NiO. A thin slice from each hot press was kept for microstructural and infrared analyses, and samples were stored in a vacuum oven at 150°C. The infrared analysis, performed using a Fourier transform infrared at the Pennsylvania State University, detected no O-H-related infrared bands in the spectra of the hot-pressed samples.

### 2.3. Deformation Apparatus and Experiments

Constant-load, triaxial compressive creep experiments were performed in a Paterson gas-medium deformation apparatus at the University of Minnesota [Paterson, 1990], courtesy of Prof. David Kohlstedt. In this

**Table 1.** Experimental Conditions for Creep of Enstatite Aggregates<sup>a</sup>

Experiment	Hot Press			Deformation				
	$P_c$ (MPa)	$T$ (°C)	$t$ (h)	$P_c$ (MPa)	$T$ Range (°C)	$\sigma$ Range (MPa)	$\epsilon_{\text{tot}}$ (%)	Grain Size ( $\mu\text{m}$ )
PI-339	300	1300	6	300	1250–1300	65–244	14	5–10 (80 vol%) 40–70 (20 vol%)
PI-402	300	1300	2	300	1200–1300	26–223	8	10–20
PI-512	450	1300	12	450	1200–1275	170–430	23	3–10
PI-539	450	1300	8	450	1200–1250	111–460	21	3–10

<sup>a</sup> $P_c$  is the confining pressure,  $T$  and  $t$  are the temperature and duration of hot press, “ $T$  range” and “ $\sigma$  range” are the ranges of temperatures and differential stresses visited during deformation, and  $\epsilon_{\text{tot}}$  is the total strain achieved.

apparatus, samples are heated using an internal furnace, limiting thermal gradients to  $<1^\circ\text{C}/\text{mm}$  and  $<4^\circ\text{C}$  over the entire hot zone of the furnace at all temperatures (up to  $1300^\circ\text{C}$ ). The applied load is measured with an internal load cell, yielding differential stresses accurate to  $\pm 2$  MPa. Sample strains are determined from piston displacement, which is measured using a linear variable differential transducer external to the pressure vessel.

For each deformation experiment, a dry hot-pressed sample was taken from the vacuum oven and placed in a nickel jacket (outer diameter 10 mm and inner diameter 8 mm). Samples were coated with NiO powder in order to buffer oxygen fugacity at Ni/NiO. Thin nickel foil disks were placed at each end of the sample to prevent chemical interactions with the rest of the assembly. The jacketed sample was placed in a piston assembly of alumina and zirconia pistons surrounded by an outer iron sleeve [Paterson and Chopra, 1982; Paterson, 1990].

Once the assembly was loaded into the deformation apparatus, pressure was increased in 10–15 MPa increments to a pressure of 300 or 450 MPa. Temperature was raised to the experimental conditions at  $\sim 1^\circ\text{C}/\text{s}$  once pressure was above 100 MPa. After the pressure and temperature conditions for the experiment were reached, the sample was allowed to equilibrate for at least 2 h before starting deformation to allow the samples to transform fully to either protoenstatite (300 MPa) or orthoenstatite (450 MPa).

Temperature calibration runs with blank assemblies were always performed prior to each series of deformation experiments. During deformation, temperature was monitored with a movable R-type thermocouple positioned within 2 mm of the sample. A temperature controller was used to maintain the temperature to within  $1^\circ\text{C}$  of the set point. Temperature profiles of the region immediately above the sample ( $\sim 5$  mm profile) were recorded periodically to verify the temperature calibration, ensuring that the sample was completely within the furnace hot zone, which did not evolve during the experiment.

The deformation experiments comprised constant-load stepping tests at temperatures from 1200 to  $1300^\circ\text{C}$  and confining pressures of either 300 MPa or 450 MPa. The applied loads were chosen to ensure that the resulting differential stresses did not significantly exceed the confining pressure, in order to minimize crack nucleation and propagation, as well as maintain the samples within the protoenstatite or the orthoenstatite fields. Measured strain rates ranged from  $10^{-6}\text{ s}^{-1}$  to  $4 \times 10^{-5}\text{ s}^{-1}$ .

In each deformation step, the applied load was held constant until an approximate steady state creep rate was achieved, typically after a strain of  $\sim 1\%$ . The load was then removed entirely before the next strain cycle. When changing temperature, the sample was allowed to anneal for  $\sim 30$  min before a new load was applied. As grain boundary migration is slow in orthopyroxene at these conditions [e.g., Skemer and Karato, 2007], no substantial grain growth was anticipated on these time scales. In most experiments, conditions of temperature and differential stress investigated in an early constant-load step were revisited later in order to test for reproducibility and to identify potential changes in mechanical behavior resulting from microstructural evolution. The total shortening strains achieved in the different experiments ranged from 8 to 23% (Table 2).

Strain rates and flow stresses were calculated from the displacement and load data, taking into account the instantaneous sample length and cross-sectional area and correcting the data for the load supported by the nickel jacket and the iron sleeve using Ni and Fe flow laws [Frost and Ashby, 1982].

#### 2.4. Microstructural and Textural Characterization

Both the starting material and the deformed samples were analyzed by optical microscopy, scanning electron microscopy (SEM) using orientation contrast (OC) and electron backscatter diffraction (EBSD), and transmission electron

**Table 2.** Creep Data for Enstatite Aggregates

Experiment	$P_c$ (MPa)	$T$ (°C)	$\sigma$ (MPa)	$\dot{\epsilon}$ ( $s^{-1}$ )	$\epsilon$ (%)			
PI-339	300	1300	229	$2.4 \pm 0.5 \times 10^{-5}$	2.0			
			197	$1.4 \pm 0.2 \times 10^{-5}$	1.1			
			169	$9.1 \pm 1.7 \times 10^{-6}$	1.3			
			130	$6.8 \pm 0.7 \times 10^{-6}$	1.1			
			108	$4.5 \pm 0.5 \times 10^{-6}$	1.2			
			86	$3.1 \pm 0.4 \times 10^{-6}$	1.0			
			65	$2.2 \pm 0.3 \times 10^{-6}$	1.0			
			221	$1.7 \pm 0.2 \times 10^{-5}$	1.5			
			244	$2.3 \pm 0.3 \times 10^{-5}$	1.6			
			164	$1.4 \pm 0.1 \times 10^{-6}$	0.9			
			193	$2.0 \pm 0.4 \times 10^{-6}$	0.9			
			225	$3.3 \pm 0.4 \times 10^{-6}$	1.0			
			PI-402	300	1299	108 <sup>a</sup>	$1.4 \pm 0.2 \times 10^{-5a}$	1.4
						55	$4.3 \pm 0.6 \times 10^{-6}$	1.0
26	$1.8 \pm 0.3 \times 10^{-6}$	1.0						
137	$1.2 \pm 0.2 \times 10^{-5}$	0.8						
82	$5.3 \pm 0.8 \times 10^{-6}$	0.9						
223	$3.2 \pm 0.5 \times 10^{-5}$	1.7						
221 <sup>b</sup>	$1.5 \pm 0.2 \times 10^{-6b}$	0.9						
PI-512	450	1200				222	$3.1 \pm 0.4 \times 10^{-6}$	1.7
			1201	$5.0 \pm 0.6 \times 10^{-6}$	1.0			
			1200	$3.36 \pm 1.0 \times 10^{-6}$	1.2			
			392	$1.3 \pm 0.2 \times 10^{-5}$	1.7			
			367	$1.1 \pm 0.2 \times 10^{-5}$	1.3			
			430	$1.8 \pm 0.3 \times 10^{-5}$	1.7			
		1250	312	$7.7 \pm 0.9 \times 10^{-6}$	1.1			
			255	$4.4 \pm 0.5 \times 10^{-6}$	1.2			
			226	$3.2 \pm 0.4 \times 10^{-6}$	1.2			
			225	$1.7 \pm 0.2 \times 10^{-5}$	1.4			
			283	$2.7 \pm 0.3 \times 10^{-5}$	1.4			
			170	$9.0 \pm 1.1 \times 10^{-6}$	1.1			
			199	$1.2 \pm 0.1 \times 10^{-5}$	1.3			
			255	$1.8 \pm 0.2 \times 10^{-5}$	1.3			
			342	$4.0 \pm 0.5 \times 10^{-5}$	1.8			
			227	$3.3 \pm 0.4 \times 10^{-5}$	1.7			
			1200	$4.06 \pm 1.2 \times 10^{-5}$	1.3			
			PI-539	450	1250	111	$2.4 \pm 0.5 \times 10^{-6}$	1.3
168	$5.6 \pm 0.8 \times 10^{-6}$	0.9						
224	$1.1 \pm 0.2 \times 10^{-5}$	1.2						
281	$2.1 \pm 0.4 \times 10^{-5}$	1.2						
334	$3.4 \pm 0.6 \times 10^{-5}$	1.5						
250	$1.5 \pm 0.2 \times 10^{-5}$	1.4						
1200	195	$8.0 \pm 1.5 \times 10^{-6}$			1.5			
	138	$3.9 \pm 0.8 \times 10^{-6}$			1.2			
	171	$1.2 \pm 0.2 \times 10^{-6}$			0.8			
	228	$2.3 \pm 0.4 \times 10^{-6}$			0.9			
	286	$4.1 \pm 0.8 \times 10^{-6}$			1.0			
	344	$7.3 \pm 1.4 \times 10^{-6}$			1.2			
1228	403	$1.3 \pm 0.2 \times 10^{-5}$			1.4			
	460	$2.3 \pm 0.3 \times 10^{-5}$			1.4			
	259	$4.4 \pm 0.7 \times 10^{-6}$			1.0			
	230	$6.8 \pm 1.2 \times 10^{-6}$			1.0			
	289	$1.3 \pm 0.1 \times 10^{-5}$			1.0			
	407	$3.6 \pm 0.6 \times 10^{-5}$			1.1			

<sup>a</sup>Transient state; discarded from data set.

<sup>b</sup>Data point in the orthoenstatite field (at 300 MPa).

microscopy (TEM). Petrographic axial sections  $\sim 20\text{--}30\ \mu\text{m}$  thick were prepared for optical microscopy. For SEM measurements, either the planar surface of an axially split sample cylinder or thin sections prepared from the samples were polished to a fine polishing grade using conventional polishing techniques and lapped with a high-pH colloidal silica suspension for several hours. The polished surfaces were not carbon coated, thereby avoiding reduction of the intensity of EBSD images. Electron charging of the uncoated samples was negligible. Samples were analyzed at the Bayerisches Geoinstitut using a Zeiss Gemini 1530 SEM with a Schottky FEG cathode operating at an accelerating voltage of 20 keV and a beam current of 2 nA at a working distance of 19 mm. Orientation contrast images were used to estimate average grain sizes in the samples before and after deformation. A topological correction factor of 1.2 was applied to determine true average grain size from grain width in the two-dimensional images. Diffraction patterns were recorded with a Nordlys II camera from HKL Technology and automatically indexed with the Channel 5 software. The patterns were recorded with large step sizes ( $20\text{--}50\ \mu\text{m}$ ) to generate pole figures describing the overall bulk texture in the samples.

Thin sections for TEM were thinned with a 5 kV argon beam, carbon coated, and investigated with a Philips CM30 transmission electron microscope operating at 300 kV, which is located at the Université de Lille.

### 3. Experimental Results

#### 3.1. Deformation Results

More than 50 creep tests were conducted on 4 enstatite samples in the protoenstatite or the orthoen-

statite field. Hot-pressing and deformation conditions are detailed in Table 1. The pressure and temperature conditions and the creep data derived from each creep test are listed in Table 2. Experiments performed at a confining pressure  $P_c$  of 300 MPa (PI-339 and PI-402) were almost entirely in the protoenstatite field or

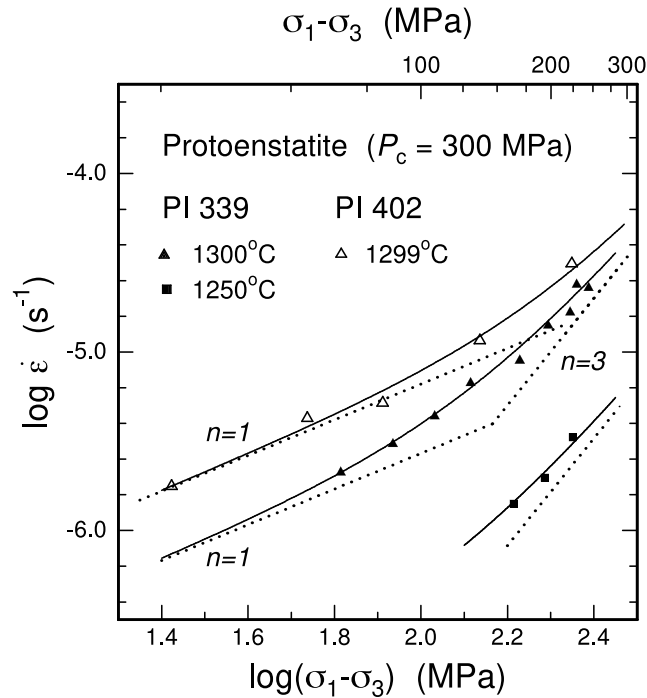


**Figure 2.** Plot of log strain rate versus log stress for creep data from experiments on dry polycrystalline enstatite deformed predominantly in the protoenstatite field. The experiments were performed using the Ni/NiO oxygen buffer at a confining pressure  $P_c$  of 300 MPa and temperatures of 1200–1300°C. Data from experiments PI-399 and PI-402 are shown as solid and open symbols, respectively. All data fall within the protoenstatite field, except for one data point at 1200°C (not shown), which was likely in the orthoenstatite field and was not used in the determination of a flow law for protoenstatite. The solid lines represent the fit of a composite flow law for dry protoenstatite at 1250 and 1300°C. The dotted lines represent the diffusal creep ( $n = 1$ ) and the dislocation creep ( $n = 3$ ) components of that flow law.

between PI-339 and PI-402 may be due to differences in grain sizes in the two samples (see section 3.2). For differential stresses above 200 MPa, where deformation becomes dominated by dislocation creep and is independent of grain size, the strengths of the two samples converge.

For most of our experimental conditions in the protoenstatite field, the samples were deformed in a mixed-mode regime, where both components contributed to creep. While it is possible that some components of grain-boundary sliding may also occur in these samples [e.g., Hirth and Kohlstedt, 2003], the data fit well to a model with only dislocation and diffusal creep components. Assuming that the diffusal and dislocation creep components are independent, the rheology of the aggregate can be described by

$$\dot{\epsilon} = \dot{\epsilon}_{\text{dif}} + \dot{\epsilon}_{\text{dis}} = A_{\text{dif}} \frac{\sigma}{d^m} \exp\left(\frac{-Q_{\text{dif}}}{RT}\right) + A_{\text{dis}} \sigma^n \exp\left(\frac{-Q_{\text{dis}}}{RT}\right), \quad (1)$$

where  $\dot{\epsilon}$  is the total strain rate;  $\dot{\epsilon}_{\text{dif}}$  and  $\dot{\epsilon}_{\text{dis}}$  are the diffusion creep and the dislocation creep rates;  $\sigma = \sigma_1 - \sigma_3$  is the differential stress;  $d$  is the grain size;  $T$  is the temperature;  $R$  is the gas constant; and  $A_{\text{dif}}$ ,  $m$ ,  $Q_{\text{dif}}$ ,  $A_{\text{dis}}$ ,  $n$ , and  $Q_{\text{dis}}$  are the empirical parameters characterizing the diffusal creep and the dislocation creep components [e.g., Poirier, 1985].

Fitting a complete flow law encompassing both the diffusal and the dislocation creep components (equation (1)) would require more measurements completely in each of the diffusal and dislocation creep fields.

possibly a mixed protoenstatite and orthoenstatite field (except for one stepping test at 1200°C, which falls within the orthoenstatite field), while experiments at  $P_c = 450$  MPa were entirely in the orthoenstatite field (Figure 1).

### 3.1.1. Protoenstatite Experiments

Strain rate versus differential stress data measured in experiments PI-339 and PI-402 in the protoenstatite field are plotted in Figure 2. At 1300°C, the deformation behavior of both samples is characterized by a low value of the apparent stress exponent ( $n \sim 1$ ) at low differential stresses and a higher value ( $n > 2$ ) at stresses above 200 MPa. Such a behavior has been observed previously for several fine grain-sized, monomineralic aggregates (e.g., olivine [Hirth and Kohlstedt, 1995a], partially molten plagioclase [Dimanov et al., 1998], and clinopyroxene [Bystricky and Mackwell, 2001]) and has been interpreted as a transition from grain boundary diffusional (Coble) creep at low stresses to a mechanism dominated by dislocation creep at high stresses. As creep rate is dependent on grain size in the diffusional creep regime, the differences in strength

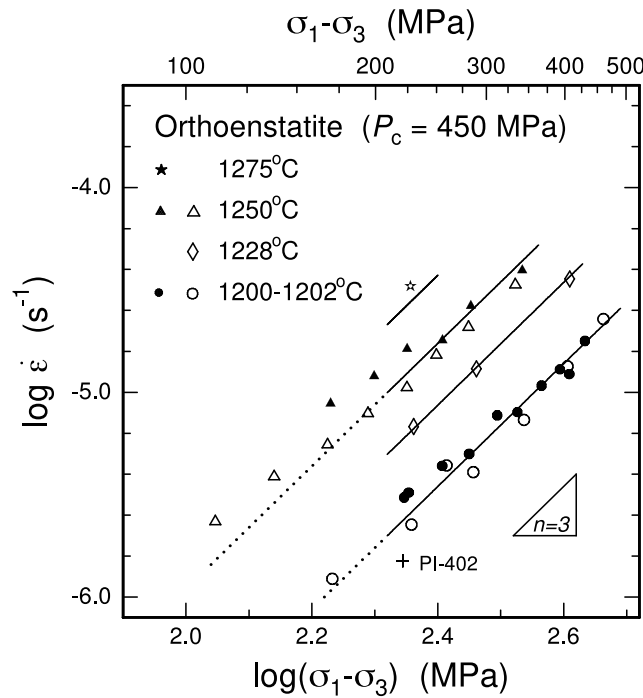


**Figure 3.** Plot of log strain rate versus log stress for creep data from experiments on dry polycrystalline enstatite deformed in the orthoenstatite field. The experiments were performed using the Ni/NiO oxygen buffer at a confining pressure  $P_c$  of 450 MPa and temperatures of 1200–1275°C. Data from experiments PI-512 and PI-539 are shown as solid and open symbols, respectively. The solid lines represent the fit of a dislocation creep flow law for dry orthoenstatite at stresses higher than 200 MPa and temperatures of 1200, 1228, 1250, and 1275°C. The dotted lines extend the flow law to lower stress conditions. The cross symbol shows the experimental result for PI-402 at a confining pressure of 300 MPa and temperature of 1200°C that fell within the orthoenstatite field.

series of solid lines for temperatures of 1250 (PI-339), 1300 (PI-339), and 1299°C (PI-402), and the individual diffusional ( $n = 1$ ) and dislocation ( $n = 3$ ) components are shown as dotted lines for the same conditions.

### 3.1.2. Orthoenstatite Experiments

Strain rate versus differential stress data measured in experiments PI-512 and PI-539, deformed within the orthoenstatite field at a confining pressure  $P_c$  of 450 MPa, are plotted in Figure 3. Results from the two experiments appear quite consistent over the range of experimental conditions. One data point for PI-402 (cross symbol in Figures 3 and 7), obtained at 1200°C and  $P_c = 300$  MPa, falls in the orthoenstatite field and demonstrates behavior reasonably consistent with the 1200°C data for PI-512 and PI-539 (Figure 3). Nonetheless, this result was not used in the rest of the analysis.

In these experiments, the contribution of diffusional creep is much smaller than in experiments in the protoenstatite field and only affects creep data at the very lowest stresses. At stresses above ~200 MPa, data show a clear linear relationship between strain rate and stress, suggesting that they can be fit to a classical Dorn-type power law constitutive equation of the form

$$\dot{\epsilon} = A_{\text{dis}} \sigma^n \exp\left(\frac{-Q_{\text{dis}}}{RT}\right). \quad (3)$$

Fits to data measured at a constant temperature and stresses higher than 200 MPa yield stress exponents between  $n = 2.8$  and 3.1. We performed global nonlinear least squares regressions on data sets at stresses above a fixed threshold (i.e., higher than 150, 200, or 250 MPa) and always obtained a stress exponent close to  $n = 3.0$ . Fixing  $n = 3$ , a global nonlinear least squares regression to the data measured at a confining

Assuming that grain size remained approximately constant in each sample during deformation at a given temperature, equation (1) can be rewritten as follows:

$$\dot{\epsilon} = K_{(T, d)} \sigma + A_{\text{dis}} \sigma^n \exp\left(\frac{-Q_{\text{dis}}}{RT}\right), \quad (2)$$

where the diffusional component of the flow law is represented by the term  $K_{(T, d)}$ , which depends on temperature and grain size (i.e., takes a constant value for each set of data points at constant temperature in a given experiment). We performed several nonlinear least squares regressions of equation (2) to the complete data set from experiments PI-339 and PI-402, using different fixed values of the stress exponent  $n$  for dislocation creep. Varying  $n$  between 3 and 4 had little effect on estimation of the activation energy for dislocation creep. For a fixed stress exponent  $n = 3$ , we obtained an activation energy  $Q_{\text{dis}} \sim 720$  kJ/mol. This value has a large uncertainty and should only be taken as an estimate. In Figure 2, the overall flow law (equation (2) using the constitutive parameters given above) is plotted as a

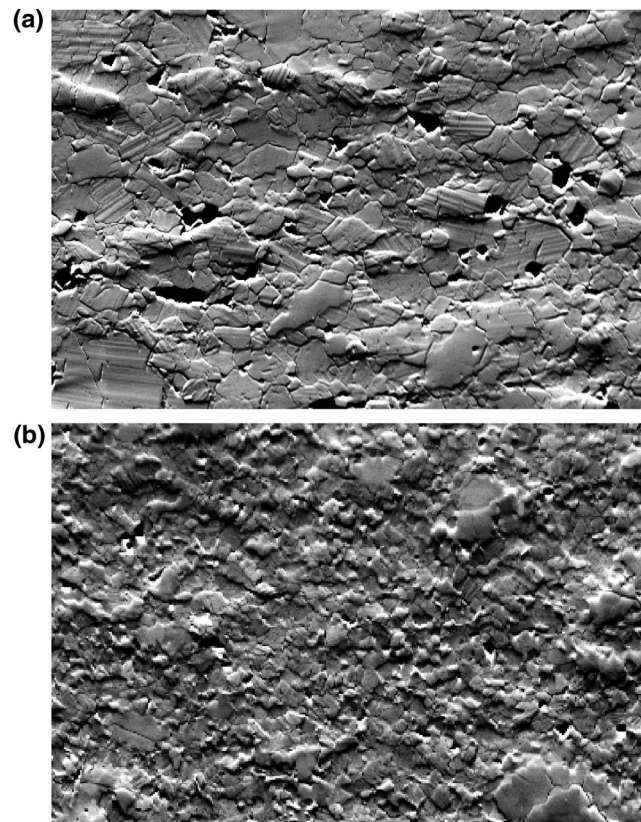


**Figure 4.** SEM orientation contrast images of deformed polycrystalline enstatite in the (a) protoenstatite and (b) orthoenstatite stability fields. Compression axis is vertical. The horizontal field of view is 130  $\mu\text{m}$ . Grain size is bimodal and dominated by a fine-grained fraction with an average grain size of  $\sim 5\text{--}10\ \mu\text{m}$  in both cases. A few larger olivine grains are visible in the microstructure deformed in the orthoenstatite stability field (e.g., bottom right corner in Figure 4b).

pressure  $P_c = 450\ \text{MPa}$  and stresses greater than 200 MPa yielded an activation energy  $Q_{\text{dis}} = 600 \pm 21\ \text{kJ/mol}$  and a preexponential term  $A_{\text{dis}} = 10^{8.63 \pm 0.73}\ \text{MPa}^{-3}\ \text{s}^{-1}$  for creep of orthoenstatite (solid lines in Figure 3). Similar activation energies  $Q_{\text{dis}}$  of  $621 \pm 22$  and  $583 \pm 23\ \text{kJ/mol}$  were determined when using only data for stresses above 150 or 250 MPa, respectively.

### 3.2. Microstructures and Textures

Optical and SEM analyses allowed phase identification, characterization of deformation processes, and grain size estimations. At the cooling rates that occur during rapid quenching from run conditions in the protoenstatite field, protoenstatite transforms mostly to low clinoenstatite [e.g., Huebner, 1980], the stable form of enstatite at low temperature and pressure (Figure 1). For the orthoenstatite samples, both high quenching rates and high stresses favor the formation of clinoenstatite lamellae within orthoenstatite grains [e.g., Buseck *et al.*, 1980]. Such transformations significantly overprint deformation microstructures, making deformation mechanism characterization challenging. In addition, stress concentrations at grain boundaries due to phase transformation and thermal stresses during quenching under load resulted in some microfracturing at grain boundaries, which caused some grain plucking during sample preparation for SEM and EBSD measurements.

#### 3.2.1. Microstructures

As anticipated, all samples recovered after deformation are composed mostly of highly twinned clinoenstatite (protoenstatite samples) [e.g., Huebner, 1980] or orthoenstatite with abundant clinoenstatite lamellae (orthoenstatite samples; Figure 4). Most of the enstatite (80–90 vol%) is fine grained with a grain size of  $3\text{--}10\ \mu\text{m}$  ( $10\text{--}20\ \mu\text{m}$  in sample PI-402). In all deformed aggregates, the fine-grained enstatite grains are elongated with their long axis perpendicular to the principal stress direction. This is particularly evident for the larger grains ( $5\text{--}20\ \mu\text{m}$ ), which have an aspect ratio of about 1:2 to 1:3, but is also true for the smallest grains.

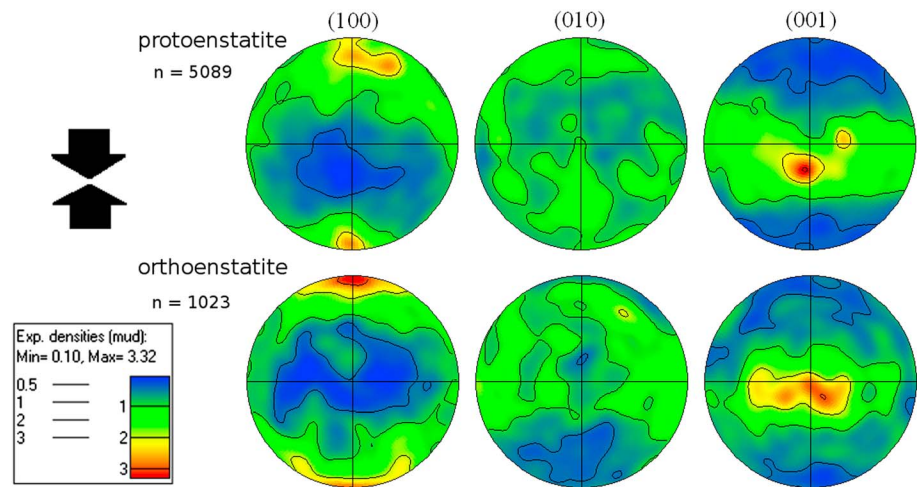


**Figure 5.** CPOs from SEM-EBSD analysis: pole figures for polycrystalline enstatite deformed in compression in the (top) protoenstatite (sample PI-339) and (bottom) orthoenstatite (sample PI-512) stability fields. Compression axis is vertical. Discrete point distributions were smoothed with a Gaussian of  $15^\circ$  in full width half maximum. The contour lines are drawn for multiples of uniform distribution (mud) equal to 0.5, 1, 2, and 3. The linear color scale indicates the low intensities in blue and high intensities in red.  $n$  indicates the number of measurements.

Samples deformed within the protoenstatite field (PI-339 and PI-402; 300 MPa) were composed entirely of enstatite with occasional distributed olivine grains (PI-339) or  $\sim 5\%$  quartz grains (PI-402). The enstatite in PI-339 has a bimodal grain size distribution, with about 20 vol% as larger grains ( $\sim 40\text{--}70\ \mu\text{m}$ ). The rest of the enstatite (80 vol%) is fine grained, with an average grain size of  $5\text{--}10\ \mu\text{m}$ . Both large and small grains have abundant clinoenstatite lamellae. The enstatite in PI-402 has a more homogeneous grain size than in PI-339, with an average grain size of  $\sim 10\text{--}20\ \mu\text{m}$ . The finely distributed quartz grains have an average grain size of about  $5\text{--}10\ \mu\text{m}$ . The differences in grain size distributions between PI-402 and PI-339 are largely due to different sample preparation methods and conditions (Table 1).

Samples deformed within the orthoenstatite field (PI-512 and PI-539; 450 MPa) contain about 10–15% olivine. The olivine grains are generally about  $15\text{--}20\ \mu\text{m}$ , with a few larger grains ( $\sim 50\ \mu\text{m}$ ). Orientation contrast (OC) imaging shows that these larger grains contain subgrains ( $\sim 15\ \mu\text{m}$ ), which are elongated perpendicular to the principal stress direction. The enstatite grains are much finer, with a grain size of  $\sim 3\text{--}10\ \mu\text{m}$ , and contain abundant clinoenstatite lamellae.

### 3.2.2. Electron Backscatter Diffraction (EBSD)

Crystallographic preferred orientations (CPOs) were measured by EBSD on samples deformed either in the protoenstatite or the orthoenstatite field (Figure 5). All the enstatite CPOs exhibit the same type of axisymmetric texture with a moderate strength (maxima in the pole figures around three multiples of uniform distribution). The (100) poles are strongly aligned with the compression direction, (001) poles tend to form a girdle normal to that direction, and the (010) distribution remains generally more diffuse. This texture is consistent with preferential slip on the easy glide system (100)[001] in protoenstatite or orthoenstatite. In sample PI-512, which contained 10–15 vol% of olivine and was deformed in the orthoenstatite field, the olivine has a CPO with [010] axes aligned with the compression direction and [100] axes perpendicular to that direction, consistent with dominant slip on the (010)[100] slip system.

### 3.2.3. High-Resolution Transmission Electron Microscopy

Transmission electron microscopy analysis of enstatite aggregates deformed either in the protoenstatite or the orthoenstatite field revealed very highly twinned grains (Figure 6). The twins are composed of alternating domains of clinoenstatite and orthoenstatite lamellae separated by (100) planes. The clinoenstatite domains are much more extensive and often appear as a clinoenstatite matrix containing very thin orthoenstatite lamellae (Figure 6a). This is especially evident in samples deformed in the protoenstatite field, where orthoenstatite planes are outnumbered by clinoenstatite planes by a ratio of about 15 to 1. Simulation of spot intensities in high-quality diffraction patterns (precession electron diffraction) confirmed that even very small grains are composed of a mixture of clinoenstatite and orthoenstatite, with a predominance of clinoenstatite.

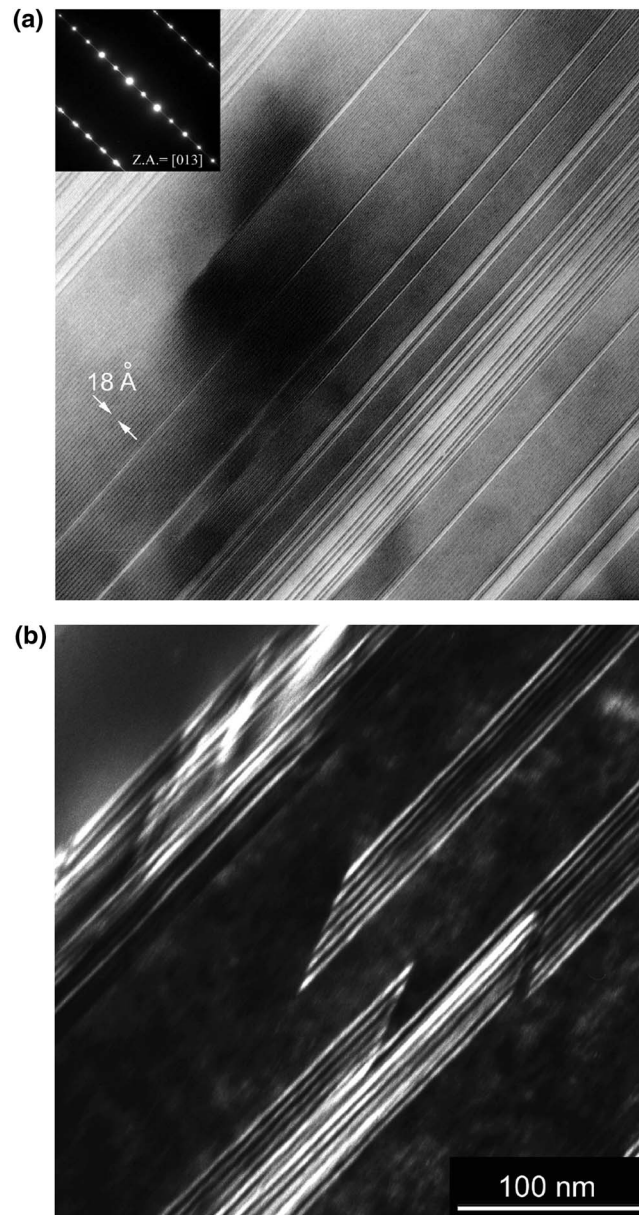


**Figure 6.** TEM micrographs of enstatite deformed in the orthoenstatite field. The deformed microstructures present (a) highly twinned grains composed of alternating domains of clinopyroxene and orthopyroxene separated by (100) planes ([013] zone axis; see the diffraction pattern in the inset). The white arrows indicate the scale (18 Å between arrows). Large domains of clinoenstatite are observed in the middle of the image, as indicated by the 4.5 Å fringe interspacing (corresponding to the so-called Si-O “plates”). Some of the twin lamellae end in the middle of grains (top left area of the image) and are limited by partial dislocations. (b) Analysis in several grains confirms that some of the (100) interphase/twin boundaries initiate inside the grains and are bound by partial *c* dislocations, suggesting extensive gliding of partial *c* dislocations in (100) planes during deformation.

In samples deformed at 300 MPa (PI-339 and PI-402), the clinoenstatite and orthoenstatite lamellae terminate on grain boundaries. By contrast, in aggregates deformed at 450 MPa (PI-512 and PI-539) the lamellae often end in the middle of grains (see top left area of Figure 6a) and are limited by partial dislocations (Figure 6b). Such features are classically observed in deformed enstatite and consist of twin lamellae bordered by partial [001] dislocations [Nazé, 1987]. Here identification of the diffraction vector *g* is consistent with these observations. We were not able to observe any free dislocations, possibly because of the very dense clinoenstatite and orthoenstatite interlayering.

## 4. Discussion

### 4.1. Microstructures, Textures, and Deformation Mechanisms

As described in section 3, all of the microstructures are mostly composed of fine-grained enstatite grains with smaller concentrations of coarser enstatite grains and olivine or quartz grains. Within the enstatite grains, polymorphism reactions are complex and greatly depend on thermodynamic conditions and factors such as cooling rate and stress state [e.g., Smith, 1969; Buseck *et al.*, 1980]. For the enstatite composition used in this study, protoenstatite directly reverts to orthoenstatite as temperature is decreased across the phase transition (~1245–1275°C at 300 MPa; Figure 1). Further cooling below ~575°C takes the enstatite into the low clinoenstatite field (Figure 1) and results in the observed alternating clinoenstatite and orthoenstatite lamellae. As observed here by TEM and noted previously by Nazé *et al.* [1987] and Mackwell [1991], dislocation microstructures resulting from high-temperature creep are at least partially overprinted by these transformation processes during quenching. Nonetheless, information on the

deformation mechanisms operative in our experiments is retained in the shape of the grains and in the EBSD signatures that record reorientation of the grains (CPO) due to dislocation glide on preferred slip systems.

While the samples deformed within the protoenstatite field are composed predominantly of fine-grained enstatite, they have some differences in chemical composition and grain-size distributions. PI-339 contains a higher concentration of large enstatite grains and minor olivine, while PI-402 contains much lower concentrations of large enstatite grains and has a modest concentration of quartz. Despite these differences, their mechanical behavior is very similar, presumably as the deformation is likely controlled by a combination of diffusional and dislocation creep in the fine-grained enstatite matrix in both cases. The similarity of deformation behavior also suggests a weak or no dependence on silica activity, in contrast to earlier results for olivine [e.g., *Bai et al.*, 1991]. However, there is insufficient data in this study to make a definitive statement on this issue. For these low-pressure experiments, the somewhat elongated grains perpendicular to the compression axis and the EBSD data suggest that dislocation creep takes place predominantly by activation of the (100) [001] slip system. As noted in *Mackwell* [1991] and *Raterron et al.* [2016], this slip system is expected to be the easiest one under our experimental deformation conditions.

The microstructures from the 450 MPa experiments, which were performed in the orthoenstatite field (Figure 1), are similar to those from the lower-pressure experiments with interlayering of intracrystalline clinoenstatite and orthoenstatite lamellae but have volumetrically more orthoenstatite than the lower-pressure experiments. Many of the planes separating the clinoenstatite and orthoenstatite layers are bordered by partial [001] dislocations, which suggests “unwinning” of orthoenstatite (i.e., partial transformation of orthoenstatite to clinoenstatite by glide of partial [001] dislocations in (100) planes), rather than a quench effect. This interpretation is corroborated by the observation that some of the clinoenstatite lamellae start in the middle of the grains, suggesting that the structure was quenched during shearing subparallel to that direction.

Similar microstructures have been observed previously both in experimentally deformed aggregates [e.g., *Coe*, 1970; *Raleigh et al.*, 1971; *Coe and Muller*, 1973; *Coe and Kirby*, 1975] and in natural samples [*Etheridge*, 1975; *van Duysen et al.*, 1985; *Nazé*, 1987; *Nazé et al.*, 1987; *Raimbourg et al.*, 2011; *Kogure et al.*, 2014]. Dissociation of [001] edge dislocations in the (100) plane, according to the reaction  $c \rightarrow 1/6 c + 5/6 c$ , is reported in association with the orthoenstatite-clinoenstatite transformation; glide of the strong  $5/6$  [001] partial dislocation then generates the unwinning of one orthorhombic unit cell into two monoclinic unit cells [*Nazé et al.*, 1987]. *Raimbourg et al.* [2011] and *Kogure et al.* [2014] identified the formation of clinoenstatite lamellae between dissociated [001] partials in orthoenstatite, leading to the development of subgrain boundaries in naturally deformed crystals. It is likely that our observations are largely due to this very mechanism, with extensive partial dislocation gliding in the (100) planes during deformation, resulting in some orthoenstatite to clinoenstatite transformation. In addition, it is consistent with the corresponding CPO, which is characteristic of slip on (100)[001] (Figure 5). These observations point to [001] dislocation glide as an important deformation mechanism in these aggregates. It also gives us confidence that the experiments were carried out in the orthoenstatite field. However, it cannot be excluded that additional clinoenstatite lamellae developed during quenching, as in the samples deformed in the protoenstatite field. Such lamellae may have erased other features, such as free dislocations and dislocation walls. Therefore, while microstructures, textures, and mechanical data ( $n=3$ ) all suggest that deformation occurred primarily in the dislocation creep field, we cannot exclude that additional deformation mechanisms were active.

In addition, the microstructures show that (second phase) olivine was also deforming by dislocation creep. The large olivine grains accommodated sufficient strain to polygonize in the finer-grained enstatite matrix, suggesting that the strength contrast between the two minerals was not that large at the conditions of deformation (see also section 4.2).

## 4.2. Mechanical Behavior and Comparison to Previous Studies

### 4.2.1. Protoenstatite Deformation

Our results for the deformation of enstatite by dislocation creep in the orthoenstatite field yielded strengths that are somewhat weaker than those measured under comparable conditions in the protoenstatite field (Figure 7). It is notable that, while PI-402 was deformed at a confining pressure of 300 MPa, the data point for 1200°C (cross symbol in Figure 7) falls within the orthoenstatite field (cf., Figure 1). The concordance of this result with the experiments at a confining pressure of 450 MPa (orthoenstatite field) provides confidence

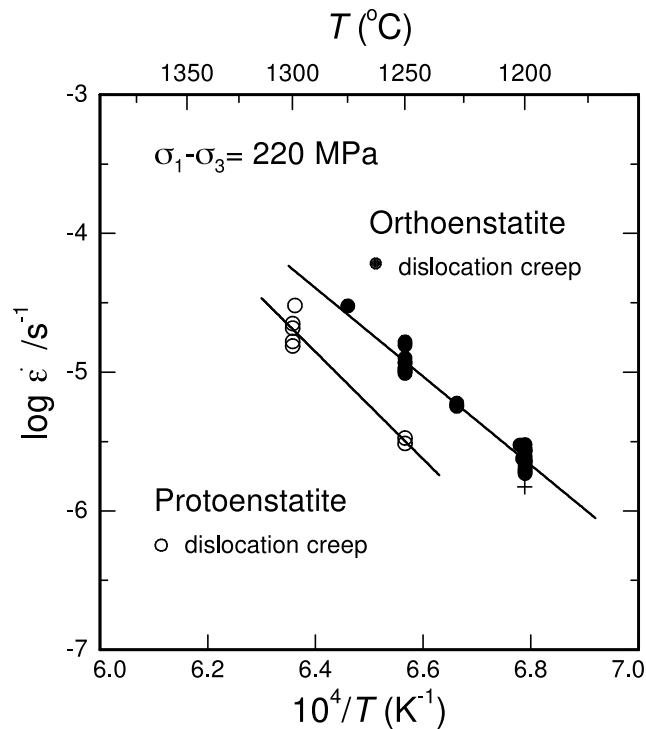


**Figure 7.** Plot of log strain rate versus inverse temperature for dislocation creep data in both the protoenstatite and orthoenstatite fields. The data were normalized to a stress of 220 MPa using a stress exponent of  $n = 3$ . The solid lines show the flow laws determined in this study for dislocation creep of dry polycrystalline enstatite in the protoenstatite and orthoenstatite fields. The cross symbol shows the experimental result for PI-402 at a confining pressure of 300 MPa and temperature of 1200°C that fell within the orthoenstatite field.

Deviations in constitutive parameters may result from the relatively narrow temperature ranges in each of the two studies and contributions of diffusional creep for the polycrystalline materials. The dotted line in Figure 8 was determined from a least squares regression fit to the results from this study and those from Mackwell [1991], yielding an “activation energy” of 820 kJ/mol. However, the requirement for deformation on multiple slip systems for homogeneous creep of a polycrystalline aggregate (von Mises criterion) limits quantitative interpretation from direct comparison of single-crystal and polycrystalline creep data. Nonetheless, it is reasonable to assume that slip on (100)[001], the weakest slip system in protoenstatite, plays an important role and may control aggregate deformation; this may explain the comparable activation energy for creep obtained for the single crystals and the aggregates.

Previous measurements on the strength of pure enstatite ( $\text{MgSiO}_3$ ) aggregates in room pressure apparatus by Ji *et al.* [2001] (*JWW*) are also shown in Figure 8. Their results are significantly weaker than ours, perhaps due to a significant component of diffusional creep in their experiments, consistent with their stress exponent of  $n = 2.0$ . Figure 8 also shows the results of Hitchings *et al.* [1989] (*HPB*) for enstatite aggregates prepared using orthopyroxene from spinel lherzolite nodules. These samples were deformed within the protoenstatite field at a temperature of 1500 K and confining pressure of 300 MPa. While the experiments yielded a stress exponent of  $n \sim 3$ , suggestive of dislocation creep, the samples had a grain size of only 5  $\mu\text{m}$  and the stress exponents were based on a single strain rate step for each experiment. Consequently, it is possible that there was some component of grain boundary diffusional creep or grain boundary sliding in the deformation behavior, which could explain the somewhat lower strength than that predicted from our experiments (Figure 8).

#### 4.2.2. Orthoenstatite Deformation

A number of prior studies have been performed in the orthoenstatite field, making use of the higher-temperature stability of orthoenstatite at higher pressures (Figure 1), such as those available in the Griggs' solid-medium deformation apparatus. Raleigh *et al.* [1971] and Ross and Nielsen [1978] performed deformation

that the transformation from protoenstatite to orthoenstatite in our experiments was relatively rapid and that our experiments were truly performed in the assumed phase fields.

Mackwell [1991] deformed single-crystal enstatite samples in the protoenstatite field at room pressure and high temperatures of between 1400 and 1450°C. These samples were oriented to favor dislocation creep on the (100)[001] slip system. While these experimental temperatures do not overlap those in the present study, the activation energies for creep of 750 and 880 kJ/mol and the stress exponent of  $n = 3.8 \pm 0.5$  obtained by Mackwell [1991] (*M*) are reasonably consistent with our high-stress results (720 kJ/mol and  $n \sim 3$ ), as illustrated in Figure 8.

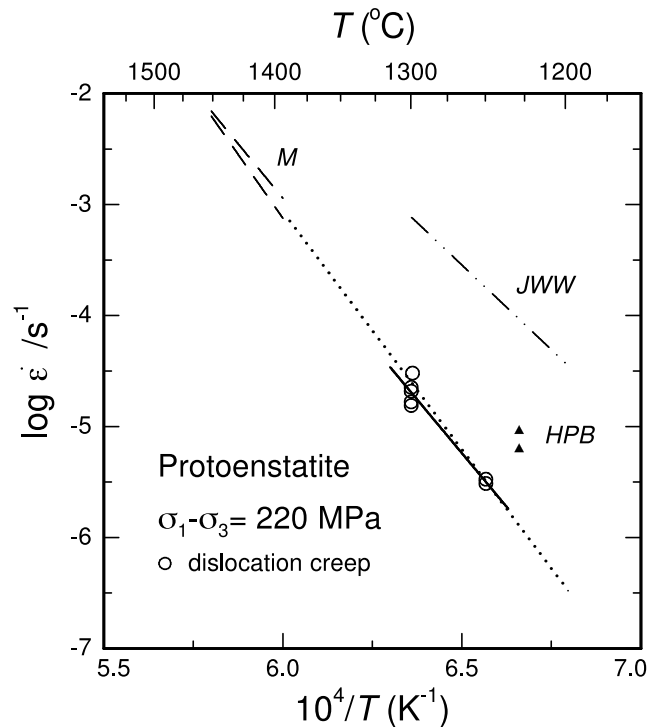


**Figure 8.** Plot of log strain rate versus inverse temperature for dislocation creep data in the protoenstatite field (circles and solid line). The data were normalized to a stress of 220 MPa using a stress exponent of  $n = 3$ . Also shown are the enstatite single-crystal (100)[001] data from Mackwell [1991] (M), the enstatite aggregate results from Hitchings et al. [1989] (HPB), and the pure MgSiO<sub>3</sub> enstatite aggregate measurements of Ji et al. [2001] (JWW). The dotted line represents a fit to the data from this study combined with the single-crystal data from Mackwell [1991]. All experiments were performed in the protoenstatite field.

conditions, and uncertainties in stress measurements caused by friction in the Griggs apparatus make it challenging to compare their data to our results. Nonetheless, as illustrated in Figure 9, there is reasonable agreement with our results in the higher-temperature region, where similar deformation mechanisms were likely to be operative. More recently, Ohuchi et al. [2011] used the Griggs' solid-medium deformation apparatus to perform experiments on oriented single crystals of enstatite at a confining pressure of 1.3 GPa and temperatures from 973 to 1373 K. Their results yield a stress exponent of  $n = 3$  and activation energy of  $Q = 459$  kJ/mol for high-temperature deformation on the (100)[001] slip system. Extrapolation of their flow law for (100)[001] to higher temperatures plots at much higher strain rates than our data and falls outside the range of strain rates plotted in Figure 9. However, as their experiments were performed in the low clinoenstatite field under wet deformation conditions and in the Griggs apparatus, it is not possible to draw serious conclusions based on the difference in behavior between their results and the data from this study and that of Mackwell [1991].

Manthilake et al. [2013] found that the (100)[001] slip system is also prevalent during deformation at 1.5 GPa and 1100°C under both dry and wet conditions. The addition of Al under dry conditions however yielded a CPO consistent with dominant activation of (010)[001]. Finally, Raterron et al. [2016] observed that the enstatite (100)[001] slip system is also prevalent over the (010)[001] slip system at higher pressures.

#### 4.2.3. Diffusional Versus Dislocation Creep

Our creep data for protoenstatite demonstrate behavior that is mostly within the diffusional creep field, although we have sufficient data to identify dislocation creep behavior at higher stresses and lower temperatures (Figure 2). By contrast, our orthoenstatite data fall mainly in the dislocation creep field but show some component of diffusional creep at lower stresses (Figure 3). In a recent study, Bruijn and Skemer [2014] used our data, together with microstructural observations, to develop a deformation mechanism map for orthopyroxene. While a more substantial data set covering a broader range of temperatures and stresses within

experiments on natural orthopyroxene aggregates under dry and wet conditions, respectively, in the solid-medium Griggs' deformation apparatus at confining pressures of 1–2 GPa. Both studies demonstrated that, at temperatures above 1000°C, deformation occurred primarily by slip on the (100)[001] system. While Ross and Nielsen [1978] acknowledged that dehydration of the talc-confining medium resulted in wet deformation conditions, Raleigh et al. [1971] used a “dry confining medium” and called their experiments dry. Nonetheless, neither study predried their orthopyroxene samples prior to deformation, so that dehydration of hydrous minerals in the aggregates inevitably resulted in nonzero water fugacities during deformation. In addition, the near coincidence of the experimental results from the two studies, both in terms of absolute strength and constitutive behavior, argues for comparable deformation conditions. The possibility that both studies were performed under wet conditions, the limited overlap in experimental

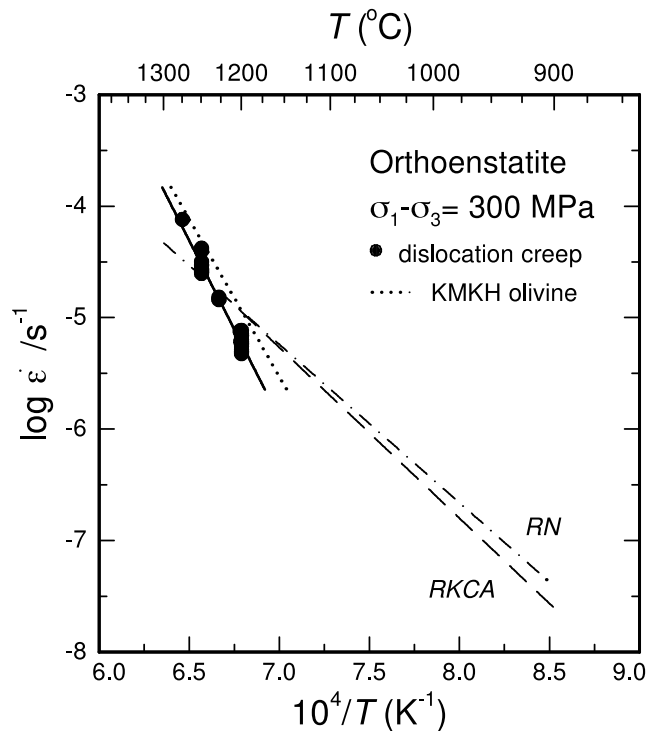


**Figure 9.** Plot of log strain rate versus inverse temperature for dislocation creep data in the orthoenstatite field. The data were normalized to a stress of 300 MPa using a stress exponent of  $n = 3$ . Also shown are the high-pressure flow laws for pyroxenite from *Raleigh et al.* [1971] (RKCA—dashed line) and *Ross and Nielsen* [1978] (RN—dot-dashed line). All experiments were performed in the orthoenstatite field. The flow law for deformation of olivine aggregates (dunite) by dislocation creep [*Keefner et al.*, 2011] is also shown for comparison (KMKH—dotted line).

to promote dislocation glide, appear weaker than olivine aggregates. Let us note however that, as mentioned above, comparing the strength of single crystals and aggregates can be highly misleading, since (i) aggregate deformation requires additional mechanisms to accommodate strain at grain boundaries and (ii) well-oriented single crystals are expected to be weaker than aggregates with random grain orientations. Figure 9 shows a comparison of our results for creep of orthoenstatite aggregates with those for dislocation creep of dry olivine aggregates (dunite) under the same conditions of temperature, confining pressure, and oxygen fugacity [*Keefner et al.*, 2011]. The orthoenstatite samples deform a factor of  $\sim 2$  slower than olivine, a result consistent with that reported by *Hitchings et al.* [1989]. It is however expected that, given the relative stress exponents and activation energies for creep, the differences in the strength of the two materials (orthopyroxene and olivine) will decrease with increasing temperature and decreasing stress.

### 4.3. Implications for Flow in the Earth

Our results are immediately applicable in regions in Earth's interior, where orthoenstatite is the dominant phase. However, much of the upper mantle is composed of aggregates with olivine as the dominant mineral and orthopyroxene in lower abundances. As noted above, dry orthoenstatite aggregates are only modestly stronger than dry olivine aggregates deformed under otherwise comparable conditions. At the lower stresses and potentially higher temperatures in the Earth's interior, orthoenstatite may be somewhat weaker or stronger than olivine, depending on the prevailing thermomechanical environment in the natural setting. Thus, previous rheologies for dry olivine aggregates [e.g., *Hirth and Kohlstedt*, 2003; *Keefner et al.*, 2011] should provide a reasonable first-order constraint on mechanical behavior for dry regions of the upper mantle. Our results are also consistent with field observations that have been interpreted variously as showing olivine weaker or stronger than enstatite [e.g., *Skemer et al.*, 2010; *Tikoff et al.*, 2010, and references therein]. It should

the appropriate phase field is desirable, such maps can be highly useful in interpreting deformation microstructures in natural rocks.

### 4.2.4. Comparison With Olivine Deformation

Olivine and orthopyroxene are the predominant minerals in mantle peridotites and lherzolites. While olivine is volumetrically dominant, the presence of orthopyroxene can have important effects on aggregate mechanical behavior, as is evidenced from numerous field observations [see, e.g., *Skemer et al.*, 2010; *Toy et al.*, 2010; *Tikoff et al.*, 2010, and references therein]. Field observations and experimental studies have attributed greater strength to either olivine or orthopyroxene, depending on the conditions of deformation. Of particular note, *Hitchings et al.* [1989] reported experiments where enstatite aggregates are similar in strength to or somewhat stronger than olivine aggregates under comparable conditions with both minerals deforming by dislocation creep. By contrast, *Ohuchi et al.* [2011] performed experiments where enstatite single crystals, oriented to

be noted, however, that our study only pertains to dry deformation and does not address the issue of water weakening of enstatite and comparison of mechanical behaviors for wet orthoenstatite and olivine.

Nonetheless, while demonstrating similar strengths under some experimental and natural conditions, olivine and enstatite do have different rheological behaviors that depend on the conditions of deformation. As is demonstrated for orthoenstatite in this study, a monomineralic rock has a unique set of constitutive parameters that define deformation for each creep field (e.g., equation (1)). These parameters quantify dependencies on the thermochemical environment, including the stress, temperature, confining pressure, oxygen and water fugacity, and activity of silica and other constituent oxides. For a rock composed of two mineral species, the constitutive parameters will not be a simple average of the parameters for each of the component minerals but reflect the individual and often complex contributions and interactions of these minerals (e.g., chemical interactions at low strains [Sundberg and Cooper, 2008] and phase mixing during dynamic recrystallization [Farla et al., 2013; Linckens et al., 2014]). Increasing temperature (as illustrated in Figure 9) and decreasing stress may result in a change from olivine to orthopyroxene as the weaker phase, with concomitant changes in stress exponent, activation energy, oxygen fugacity exponent, and other constitutive parameters for an aggregate composed of the two minerals. In addition, deformation may also lead to different recrystallized grain sizes for olivine and for orthopyroxene, possibly causing a switch in deformation mechanism from dislocation to diffusional creep in orthopyroxene and thereby extending the range of conditions where orthopyroxene is the weaker mineral [Skemer and Karato, 2008]. Consequently, a laboratory-based rheology for such a bimineralic rock cannot be reliably extrapolated to natural deformation conditions. Instead, flow laws should be measured for each mineral component, which can then be extrapolated and compared to determine the contribution of each to the local deformation. Careful measurement of deformation in single crystals or monomineralic aggregates, coupled with experiments and simulations of bimineralic or polymineralic systems [e.g., Tullis et al., 1991; Handy, 1994; Raterron et al., 2014; Hansen and Warren, 2015, and references therein], can provide insight into appropriate rheologies for use in a variety of natural settings.

#### Acknowledgments

This research was supported by the Geophysics Program in EAR at NSF. We wish to thank David Kohlstedt for his generous support throughout this research and P. Skemer and B. Holtzman for their thoughtful comments on this manuscript. J.L. and S.M. are grateful for the support from NSF (EAR-9018044) and NASA (NNX08AC28A). This paper is LPI contribution 1862. F.H. gratefully acknowledges support through DFG grant He3258/2-1. The TEM national facility in Lille (France) is supported by the Conseil Regional du Nord-Pas de Calais, the European Regional Development Fund, and the Institut National des Sciences de l'Univers (CNRS). The data used are listed in the tables and shown in the figures.

#### References

- Amiguet, E., P. Raterron, P. Cordier, H. Couvy, and J. Chen (2009), Deformation of diopside single crystal at mantle pressure. 1: Mechanical data, *Phys. Earth Planet. Inter.*, *177*, 122–129, doi:10.1016/j.pepi.2009.08.010.
- Amiguet, E., P. Cordier, and P. Raterron (2010), Deformation of diopside single crystals at mantle pressure. TEM characterization of dislocation microstructures, *Eur. J. Mineral.*, *22*, 181–187, doi:10.1127/0935-1221/2010/0022-1995.
- Avé Lallemant, H. G. (1978), Experimental deformation of diopside and websterite, *Tectonophysics*, *48*, 1–27.
- Bai, Q., S. J. Mackwell, and D. L. Kohlstedt (1991), High-temperature creep of olivine single crystals 1. Mechanical results for buffered samples, *J. Geophys. Res.*, *96*, 2441–2463, doi:10.1029/90JB01723.
- Boland, J. N., and T. E. Tullis (1986), Deformation behavior of wet and dry clinopyroxenite in the brittle to ductile transition region, in *Mineral and Rock Deformation: Laboratory Studies*, edited by B. E. Hobbs and H. C. Heard, pp. 35–49, AGU, Washington, D. C.
- Borch, R. S., and H. W. Green II (1989), Deformation of peridotite at high pressure in a new molten salt cell: Comparison of traditional and homologous temperature treatments, *Phys. Earth Planet. Inter.*, *55*, 269–276.
- Brujijn, H. C., and P. Skemer (2014), Grain-size sensitive rheology of orthopyroxene, *Geophys. Res. Lett.*, *41*, 4894–4903, doi:10.1002/2014GL060607.
- Buseck, P. R., G. L. Nord Jr., and D. R. Veblen (1980), Subsolidus phenomena in pyroxenes, in *Pyroxenes, Rev. in Mineral and Geochem.*, vol. 4, chap. 4, pp. 117–211, MSA, Chantilly, Va.
- Bystricky, M., and S. Mackwell (2001), Creep of dry clinopyroxene aggregates, *J. Geophys. Res.*, *106*, 13,443–13,454, doi:10.1029/2001JB000333.
- Bystricky, M., K. Kunze, L. Burlini, and J.-P. Burg (2000), High shear strain of olivine aggregates: Rheological and seismic consequences, *Science*, *290*, 1564–1567.
- Carter, N. L., and H. G. Avé Lallemant (1970), High temperature flow of dunite and peridotite, *Geol. Soc. Am. Bull.*, *81*, 2181–2202.
- Chen, S., T. Hiraga, and D. L. Kohlstedt (2006), Water weakening of clinopyroxene in the dislocation creep regime, *J. Geophys. Res.*, *111*, B08203, doi:10.1029/2005JB003885.
- Chopra, P. N., and M. S. Paterson (1981), The experimental deformation of dunite, *Tectonophysics*, *78*, 453–473.
- Chopra, P. N., and M. S. Paterson (1984), The role of water in the deformation of dunite, *J. Geophys. Res.*, *89*, 7861–7876, doi:10.1029/JB089iB09p07861.
- Coe, R. S. (1970), The thermodynamic effect of shear stress on the ortho-clino inversion in enstatite and other coherent phase transitions characterized by a finite simple shear, *Contrib. Mineral. Petrol.*, *26*, 247–264.
- Coe, R. S., and S. H. Kirby (1975), The orthoenstatite to clinoenstatite transformation by shearing and reversion by annealing: Mechanism and potential applications, *Contrib. Mineral. Petrol.*, *52*, 29–55.
- Coe, R. S., and W. F. Muller (1973), Crystallographic orientation of clinoenstatite produced by deformation of orthoenstatite, *Science*, *180*, 64–66.
- Dehghan, A., C. G. Sammis, and T. G. Langdon (1981), High temperature deformation of polycrystalline orthoenstatite under controlled oxygen fugacity, *Eos Trans. AGU*, *62*, 1029.
- Dehghan, A., T. G. Langdon, and C. G. Sammis (1982), High temperature creep of polycrystalline orthoenstatite, *Eos Trans. AGU*, *63*, 1094.
- Dimanov, A., G. Dresen, and R. Wirth (1998), High-temperature creep of partially molten plagioclase aggregates, *J. Geophys. Res.*, *103*, 9651–9664, doi:10.1029/97JB03742.

- Durham, W. B., S. Mei, D. L. Kohlstedt, L. Wang, and N. A. Dixon (2009), New measurements of activation volume in olivine under anhydrous conditions, *Phys. Earth Planet. Inter.*, *172*, 67–73, doi:10.1016/j.pepi.2008.07.045.
- Etheridge, M. A. (1975), Deformation and recrystallisation of orthopyroxene from the Giles Complex, central Australia, *Tectonophysics*, *25*, 87–114.
- Farla, R. J., S. Karato, and Z. Cai (2013), Role of orthopyroxene in rheological weakening of the lithosphere via dynamic recrystallization, *Proc. Natl. Acad. Sci. U.S.A.*, *110*(41), 16,355–16,360, doi:10.1073/pnas.1218335110.
- Frost, H. J., and M. F. Ashby (1982), *Deformation-Mechanism Maps: The Plasticity and Creep of Metals and Ceramics*, 167 pp., Pergamon, New York.
- Gasparik, T. (2003), *Phase Diagrams for Geoscientists, an Atlas of the Earth's Interior*, 462 pp., Springer, Berlin.
- Handy, M. R. (1994), Flow laws for rocks containing two non-linear viscous phases: A phenomenological approach, *J. Struct. Geol.*, *16*, 287–301.
- Hansen, L. N., and J. M. Warren (2015), Quantifying the effect of pyroxene on deformation of peridotite in a natural shear zone, *J. Geophys. Res. Solid Earth*, *120*, 2717–2738, doi:10.1002/2014JB011584.
- Hier-Majumder, S., S. Mei, and D. L. Kohlstedt (2005), Water weakening of clinopyroxenite in diffusion creep, *J. Geophys. Res.*, *110*, B07406, doi:10.1029/2004JB003414.
- Hirth, G., and D. L. Kohlstedt (1995a), Experimental constraints on the dynamics of the partially molten upper mantle: Deformation in the diffusion creep regime, *J. Geophys. Res.*, *100*, 1981–2001, doi:10.1029/94JB02128.
- Hirth, G., and D. L. Kohlstedt (1995b), Experimental constraints on the dynamics of the partially molten upper mantle, 2. Deformation in the dislocation creep regime, *J. Geophys. Res.*, *100*, 15,441–15,449, doi:10.1029/95JB01292.
- Hirth, G., and D. L. Kohlstedt (2003), Rheology of the upper mantle and the mantle wedge: A view from the experimentalists, in *Inside the Subduction Factory, Geophys. Monogr. Ser.*, vol. 138, edited by J. Eiler, pp. 83–105, AGU, Washington, D. C.
- Hitchings, R. S., M. S. Paterson, and J. Bitmead (1989), Effects of iron and magnetite additions in olivine-pyroxene rheology, *Phys. Earth Planet. Inter.*, *55*, 277–291.
- Huebner, J. S. (1980), Pyroxene phase equilibria at low pressure, in *Pyroxenes, Rev. in Mineral.*, vol. 7, edited by C. T. Prewitt, pp. 213–288, Mineral. Soc. Am., Washington, D. C.
- Ingrin, J., N. Doukhan, and J. C. Doukhan (1991), High-temperature deformation of diopside single crystal, 2. TEM investigation of the induced defect microstructures, *J. Geophys. Res.*, *96*, 14,287–14,297, doi:10.1029/91JB01233.
- Ingrin, J., N. Doukhan, and J. C. Doukhan (1992), Dislocation glide systems in diopside single crystals deformed at 800–900°C, *Eur. J. Mineral.*, *4*, 1291–1302.
- Jaoul, O., and P. Paterson (1994), High-temperature deformation of diopside crystal 3. Influences of  $pO_2$  and  $SiO_2$  precipitation, *J. Geophys. Res.*, *99*, 9423–9439, doi:10.1029/93JB03363.
- Ji, S. C., Z. Wang, and R. Wirth (2001), Bulk flow strength of forsterite-enstatite composites as a function of forsterite content, *Tectonophysics*, *341*, 69–93.
- Karato, S., and H. Jung (2003), Effects of pressure on high-temperature dislocation creep in olivine, *Philos. Mag.*, *83*, 401–414, doi:10.1080/0141861021000025829.
- Karato, S., M. S. Paterson, and J. D. Fitz Gerald (1986), Rheology of synthetic olivine aggregates: Influence of grain size and water, *J. Geophys. Res.*, *91*, 8151–8179, doi:10.1029/JB091iB08p08151.
- Keefner, J. W., S. J. Mackwell, D. L. Kohlstedt, and F. Heidelbach (2011), Dependence of dislocation creep of dunite on oxygen fugacity: Implications for viscosity variations in Earth's mantle, *J. Geophys. Res.*, *116*, B05201, doi:10.1029/2010JB007748.
- Kirby, S. H., and A. K. Kronenberg (1984), Deformation of clinopyroxenite: Evidence for a transition in flow mechanisms and semibrittle behavior, *J. Geophys. Res.*, *89*, 3177–3192, doi:10.1029/JB089iB05p03177.
- Kogure, T., H. Raimbourg, A. Kumamoto, E. Fujii, and Y. Ikuhara (2014), Subgrain boundary analyses in deformed orthopyroxene by TEM/STEM with EBSD-FIB sample preparation technique, *Earth Planets Space*, *66*, 84, doi:10.1186/1880-5981-66-84.
- Kollé, J. J., and J. D. Blacic (1982), Deformation of single-crystal clinopyroxenes: 1. Mechanical twinning in diopside and hedenbergite, *J. Geophys. Res.*, *87*, 4019–4034, doi:10.1029/JB087iB05p04019.
- Kollé, J. J., and J. D. Blacic (1983), Deformation of single-crystal clinopyroxenes: 2. Dislocation-controlled flow processes in hedenbergite, *J. Geophys. Res.*, *88*, 2381–2393, doi:10.1029/JB088iB03p02381.
- Lawlis, J. D. (1998), High temperature creep of synthetic olivine-enstatite aggregates, PhD thesis, 133 pp., Pa. State Univ., University Park.
- Linckens, J., R. H. C. Bruijn, and P. Skemer (2014), Dynamic recrystallization and phase mixing in experimentally deformed peridotite, *Earth Planet. Sci. Lett.*, *388*, 134–142, doi:10.1016/j.epsl.2013.11.037.
- Mackwell, S. J. (1991), High-temperature rheology of enstatite: Implications for creep in the mantle, *Geophys. Res. Lett.*, *18*, 2027–2030, doi:10.1029/91GL02492.
- Mackwell, S. J., D. L. Kohlstedt, and M. S. Paterson (1985), The role of water in the deformation of olivine single crystals, *J. Geophys. Res.*, *90*, 11,319–11,333, doi:10.1029/JB090iB13p11319.
- Manthilake, M. A. G. M., N. Miyajima, F. Heidelbach, V. Soustelle, and D. J. Frost (2013), The effect of aluminum and water on the development of deformation fabrics in orthopyroxene, *Contrib. Mineral. Petrol.*, *165*, 495–505, doi:10.1007/s00410-012-0819-4.
- Mauler, A., M. Bystricky, K. Kunze, and S. J. Mackwell (2000), Microstructures and lattice preferred orientations in clinopyroxene aggregates experimentally deformed in compression and torsion, *J. Struct. Geol.*, *22*, 1633–1648.
- McDonnell, R. D., C. J. Peach, H. L. M. van Roermund, and C. J. Spiers (2000), Effect of varying enstatite content on the deformation of fine-grained synthetic peridotite under wet conditions, *J. Geophys. Res.*, *105*, 13,535–13,553, doi:10.1029/1999JB900412.
- Mei, S., and D. L. Kohlstedt (2000a), Influence of water on plastic deformation of olivine aggregates. 1. Diffusion creep regime, *J. Geophys. Res.*, *105*, 21,457–21,469, doi:10.1029/2000JB900179.
- Mei, S., and D. L. Kohlstedt (2000b), Influence of water on plastic deformation of olivine aggregates. 2. Dislocation creep regime, *J. Geophys. Res.*, *105*, 21,471–21,481, doi:10.1029/2000JB900180.
- Nazé, L. (1987), Etude par microscopie électronique en transmission des défauts de réseau dans les orthopyroxènes déformés naturellement et expérimentalement, Thèse de Doctorat, no. d'ordre 177, 163 pp., Univ. des Scie. et Technol. de Lille Flandres Artois.
- Nazé, L., N. Doukhan, J.-C. Doukhan, and K. Latrous (1987), A TEM study of lattice defects in naturally and experimentally deformed orthopyroxenes, *Bull. Mineral.*, *110*, 497–512.
- Ohuchi, T., S. Karato, and K. Fujino (2011), Strength of single-crystal orthopyroxene under lithospheric conditions, *Contrib. Mineral. Petrol.*, *161*, 961–975, doi:10.1007/s00410-010-0574-3.
- Paterson, M. S. (1990), Rock deformation experimentation, in *Brittle-Ductile Transition in Rocks, Geophys. Monogr. Ser.*, vol. 56, edited by A. G. Duba et al., pp. 187–194, AGU, Washington, D. C.
- Paterson, M. S., and P. N. Chopra (1982), The jacketing of specimens in high-temperature, high-pressure rock-deformation experiments, *High Temp. High Pressures*, *14*, 315–318.

- Poirier, J.-P. (1985), *Creep of Crystals*, 260 pp., Cambridge Univ. Press, New York.
- Raimbourg, H., T. Kogure, and T. Toyoshima (2011), Crystal bending, subgrain boundary development, and recrystallization in orthopyroxene during granulite-facies deformation, *Contrib. Mineral. Petrol.*, *162*, 1093–1111, doi:10.1007/s00410-011-0642-3.
- Raleigh, C. B., S. H. Kirby, N. L. Carter, and H. G. Avé Lallemant (1971), Slip and clinoenstatite transformation as competing rate processes in enstatite, *J. Geophys. Res.*, *76*, 4011–4022, doi:10.1029/JB076i017p04011.
- Raterron, P., and O. Jaoul (1991), High-temperature deformation of diopside single crystal, 1. Mechanical data, *J. Geophys. Res.*, *96*, 14,277–14,286, doi:10.1029/91JB01205.
- Raterron, P., N. Doukhan, O. Jaoul, and J. C. Doukhan (1994), High-temperature deformation of diopside IV: Predominance of {110} glide above 1000°C, *Phys. Earth Planet. Inter.*, *82*, 209–222.
- Raterron, P., E. Amiguet, J. Chen, L. Li, and P. Cordier (2009), Experimental deformation of olivine single crystals at mantle pressures and temperatures, *Phys. Earth Planet. Inter.*, *172*, 74–83, doi:10.1016/j.pepi.2008.07.026.
- Raterron, P., F. Detrez, O. Castelnau, C. Bollinger, P. Cordier, and S. Merkel (2014), Multiscale modeling of upper mantle plasticity: From single-crystal rheology to multiphase aggregate deformation, *Phys. Earth Planet. Inter.*, *228*, 232–243, doi:10.1016/j.pepi.2013.11.012.
- Raterron, P., G. Frayse, J. Girard, and C. Holyoke III (2016), Strength of orthoenstatite single crystals at mantle pressure and temperature and comparison with olivine, *Earth Planet. Sci. Lett.*, *450*, 326–336, doi:10.1016/j.epsl.2016.06.025.
- Ross, J. V., and K. C. Nielsen (1978), High-temperature flow of wet polycrystalline enstatite, *Tectonophysics*, *44*, 233–261.
- Schloessin, H. H., and G. Ranalli (1988), Hot creep of single-crystals by bending: Procedure, theory and pilot experiment on enstatite, *Phys. Earth Planet. Inter.*, *52*, 132–149.
- Skemer, P., and S. Karato (2007), Effects of solute segregation on the grain-growth kinetics of orthopyroxene with implications for the deformation of the upper mantle, *Phys. Earth Planet. Inter.*, *164*, 186–196, doi:10.1016/j.pepi.2007.06.011.
- Skemer, P., and S. Karato (2008), Sheared Iherzolite xenoliths revisited, *J. Geophys. Res.*, *113*, B07205, doi:10.1029/2007JB005286.
- Skemer, P., J. M. Warren, P. B. Kelemen, and G. Hirth (2010), Microstructural and rheological evolution of a mantle shear zone, *J. Petrol.*, *51*, 43–53, doi:10.1093/ptrology/egp057.
- Smith, J. V. (1969), Magnesium pyroxenes at high temperature: Inversion in clinoenstatite, *Nature*, *222*, 256–257.
- Sundberg, M., and R. F. Cooper (2008), Crystallographic preferred orientation produced by diffusional creep of harzburgite: Effects of chemical interactions among phases during plastic flow, *J. Geophys. Res.*, *113*, B12208, doi:10.1029/2008JB005618.
- Tikoff, B., C. E. Larson, J. Newman, and T. Little (2010), Field-based constraints on finite strain and rheology of the lithospheric mantle, Twin Sisters, Washington, *Lithosphere*, *2*, 418–422, doi:10.1130/L97.1.
- Toy, V. G., J. Newman, W. Lamb, and B. Tikoff (2010), The role of pyroxenites in formation of shear instabilities in the mantle: Evidence from an ultramafic ultramylonite, Twin Sisters Massif, Washington, *J. Petrol.*, *51*, 55–80, doi:10.1093/ptrology/egp059.
- Tullis, T. E., F. G. Horowitz, and J. Tullis (1991), Flow laws of polyphase aggregates from end-member flow laws, *J. Geophys. Res.*, *96*, 8081–8096, doi:10.1029/90JB02491.
- van Duysen, J. C., N. Doukhan, and J. C. Doukhan (1985), Transmission electron microscope study of dislocations in orthopyroxene (Mg,Fe)<sub>2</sub>Si<sub>2</sub>O<sub>6</sub>, *Phys. Chem. Miner.*, *12*, 39–44.
- Zeuch, D. H., and H. W. Green (1984), Experimental deformation of a synthetic dunite at high temperature and pressure 1. Mechanical behavior, optical microstructure and deformation mechanisms, *Tectonophysics*, *110*, 233–262.